A 2D full-waveform inversion using trench-deployed surface and VSP DAS data from CaMI FRS

Luping Qu, Wenyong Pan, Kris Innanen

ABSTRACT

Based on the previous surface-wave full-waveform inversion (FWI). A full-waveform inversion using trench-deployed surface waves and two wells' Vertical Seismic Profiling (VSP) data was conducted to generate a high-resolution S- and P-wave velocity models of the near surface at Containment and Monitoring Institute Field Research Station in Alberta. In this preliminary inversion, a sequential inversion was conducted by firstly inverting Vs using surface-wave FWI, and secondly inverting Vp using the VSP FWI. There are two datasets collected in August 2022 for the main CO_2 monitoring line, line 13. They possess the same frequency range, with linear and low-dwell sweep, respectively. In this study, we compared these two datasets in detail. The inversion results are from the DAS data generated using the low-dwell sweep. Optical transport method was adopted to mitigate the cycle skipping problem mainly in surface wave inversion.

INTRODUCTION

CaMI FRS

The Containment and Monitoring Institute Field Research Station (CaMI-FRS) in Newell County (Figure 1), Alberta, Canada, is a unique facility designed to support the development of monitoring and verification technologies related to carbon capture and storage, and other containment and conformance requirements (such as CO_2 enhanced oil recovery)(Lawton et al., 2019). At the FRS, small and controlled amounts of CO_2 are being injected into the shallow Basal Belly River Sandstone Formation at 300 m depth. A variety of geophysical sensing technologies have been deployed at or near the surface of the 1 km by 1 km facility, or within one of the two observation wells, to facilitate development of monitoring methods. This includes a 3D array of 3C geophones (Lawton et al., 2015); 3 permanent mounted vibratory sources (Spackman and Lawton, 2018); 7 broadband seismic stations (Stork et al., 2018); and a 5 km loop of both straight and helically-wound distributed acoustic sensing (DAS) fibre, and 2 observation wells (Gordon and Lawton, 2017, 2018; Hall et al., 2017; Lawton et al., 2018; Hall et al., 2018).

DAS is a novel technology for seismic acquisition that measures phase changes of back-scattered laser pulses (Rayleigh scattering) induced by transient vibrations incident on optical fibers (Posey et al., 2000; Masoudi et al., 2013). The phase changes are proportional to axial strain changes along finite segments of the fiber, referred to as *gauge length*. Therefore, strain rate (or strain) changes along the fiber are recorded. Compared to standard geophones, DAS has a series of advantages including dense spatial sampling, low-cost, easy installation, etc. Recent studies also revealed that the optical fibers show high sensitivity to low-frequency signals (Lindsey et al., 2017; Jin and Roy, 2017). It is particularly useful for real-time, high-resolution, and long-term seismic monitoring applications. For examples, DAS has been successfully applied to down-hole reservoir monitoring (Masoudi et al., 2014;

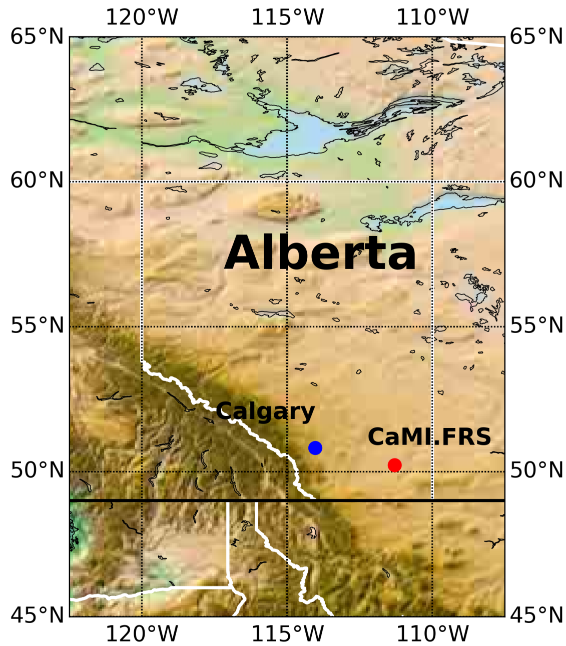

FIG. 1. The location of CaMI Field Research Station

Daley et al., 2016), near-surface characterization and S-wave velocity V_S imaging (Dou et al., 2017; Ajo-Franklin et al., 2019), illuminating seafloor faults and ocean dynamics (Lindsey et al., 2019).

The DAS fibre includes a 1.1 km horizontal section in a trench that is considered in our work. In 2018, a surface wave data set was recorded for source positions along the 1.1 km trenched segment of the DAS fibre. These data provide us with an opportunity to study the estimation of S-wave velocity models using multiple surface wave modes, sensed by the DAS fibre, by applying a TD Bayesian inversion methodology. In August, 2022, more datasets were collected from the field data tests. Over 100 shots were collected from the line 13 using both linear sweep VP and low-dwell sweep VP, with the frequency range of 2-150 Hz. 10 shots with high Signal-to-Noise Ratio (SNR) were selected from these data. The geometry is shown in Figure 4.

Surface-wave FWI

High-amplitude, dispersive surface waves, that decay exponentially with depth and have the majority of their energy contained within a depth of only about half a wavelength from the free surface, are the dominant seismic traces in land surveys. Surface waves are frequently treated as noise in seismic exploration studies for imaging deeper structures, despite their use in other fields such as ultrasonic acoustics, geotechnical engineering, nondestructive testing, archaeological studies, near-surface geophysics, and global seismology (Socco et al., 2010). Migration imaging using weaker reflected signals necessitates the mitigation of this noise, but it can be difficult due to the multiple modes of propagation of surface waves, each of which has unique dispersive properties. In the DAS dataset collected from the field, we found there is no obvious reflection waves at the horizontal components due to

DAS acquisition principle. Thus we resort to use multimode surface waves as our signals to obtain the near-surface velocity profile.

Surface wave multichannel analysis (Park et al., 1999; Xia et al., 1999) and spectral analysis (Nazarian and Stokoe, 1984) are common techniques for near-surface inversion. Construction of local 1D profiles can be facilitated by dispersion curve analyses using f-k or Radon transforms for a multichannel array, but they are inherently incapable of handling lateral variations. FWI is a more versatile method for handling surface waves because, in theory, it can create high-resolution models using the entire wavefield captured by seismograph. By utilizing all of the wave modes present in the data, full waveform inversion (FWI) of surface wave data tries to recover the elastic properties of the near-surface. However, in FWI, when the initial model is not close to the true model, cycle skipping due to the non-convexity of FWI problem can happen, which is related to the oscillatory nature of seismic data. The cycle skipping issue is amplified by the surface wave's dispersive nature and its shorter wavelengths. Alternative misfit functions have been suggested as a solution (Borisov et al., 2018; Yuan et al., 2015; Masoni et al., 2013; Pérez Solano et al., 2014). Following a layer-stripping methodology, Masoni et al. (2016) move from narrow-offset high-frequency components, which provide information about the shallower parts of the near-surface, to wide-offset low-frequency components, which do the same for the lower part of the near-surface.

An alternative method to mitigate cycle skipping is optical transport (OT). The idea is to take advantage of the inherent convexity of optimal transport distances with respect to translation and dilation. Engquist and Froese firstly introduced the idea of using optimal transport for seismic inversion (2014). Optimal transportation is the basis of the Wasserstein metric (Villani, 2003). Here, we treat our seismic signal data sets as density functions of two probability distributions, which are represented by the distributions of two equal-mass sand piles. Different strategies for moving one pile into the other result in different costs when compared to the same cost function. The optimal map is the plan with the lowest cost, which is determined by the Wasserstein metric. The metric is frequently referred to as the "earth mover's distance" in computer science. We will concentrate on quadratic cost functions in this section. The quadratic Wasserstein metric is the corresponding misfit. Geophysics researchers began focusing on other optimal transport-related misfit functions following the publication of Engquist and Froese's (2014) paper (Métivier et al., 2016a, 2016b, 2016c). The Kantorovich-Rubinstein (KR) norm in their papers is a relaxation of the 1-Wasserstein distance, which is another optimal transport metric with the absolute value cost function. The KR norm has the benefit of not requiring information to satisfy nonnegativity or mass balance conditions.

VSP FWI

In order to obtain a velocity model at deeper zones with high solution and accuracy, larger offsets are usually required and a higher domain frequency (Sirgue, 2004; Mulder, 2008; Operto, 2009). However, for surface acquisition, the maximum offset and domain frequency are limited. Which can result in low resolution of the inversion result close to the model's edges (Hou, et al., 2012).

The vertical seismic profiling (VSP) data are often used as a tool for high-resolution imaging in areas where surface seismic resolution is low. VSP data can potentially provide higher-resolution images compared to surface seismic data because VSP receivers are closer to the target, and the reflected energy travels only once through the weathering layer, leading to fewer high-frequency losses (Blias., 2015). In addition to the obvious disadvantage of VSP having a limited illumination zone constrained by the well location.

METHOD

Full-waveform inversion in isotropic-elastic media

In a typical FWI formulation, model parameters are iteratively updated by minimizing the direct waveform-difference (WD) between the synthetic data u_i and observed seismic data d_i, which can be formulated as a L-2 norm misfit, e.g.,

$$\Phi\left(\mathbf{m}\right) = \frac{1}{2}\sum_{r=1}^{N_r}\int_0^{t'}\int_V \left[u_i\left(\mathbf{x}_r, t; \mathbf{m}\right) - d_i\left(\mathbf{x}_r, t\right)\right]^2 d\mathbf{x}dt, \tag{1}$$

where $\mathbf{m}$ is the model vector, $\mathbf{x}_r$ indicates the rth receiver location with a maximum number of N_r, t' is the maximum recording time and V denotes the whole volume containing all subsurface positions $\mathbf{x}$. In purely elastic media without considering anisotropy and attenuation, V_S sensitivity kernel (or gradient) of the misfit function can be calculated by cross-correlating the forward and adjoint wavefields based on the adjoint-state method (Liu and Tromp, 2006; Plessix, 2006):

$$K_{V_S} = -\sum_{r=1}^{N_r}\int_0^{t'}\int_V 2\rho V_S^2\left[\partial_j u_i^{\dagger}\left(\partial_i u_j + \partial_j u_i\right) - 2\partial_i u_i^{\dagger}\partial_k u_k\right] d\mathbf{x}dt, \tag{2}$$

where ρ is the mass density, $u_i^{\dagger}$ indicates the adjoint displacement wavefield, the subscripts i, j and k take on the values of x and z for 2D media. In equation (2), we ignore the dependence of wavefields on time, space and receivers for sake of compactness. We apply l-BFGS optimization and line search methods to calculate the search directions and step lengths (Nocedal and Wright, 2006) for updating the model iteratively. In this study, the WD misfit function is applied to surface-waves recorded on surface-trenched fibers at CaMI.FRS for obtaining a near-surface V_S model.

Optimal Transport

OT-based misfits can be interesting for FWI as they exhibit a wider convexity with respect to time shifts. Various formulations of OT applied to FWI exist, and all are related to Wasserstein distances. The p-Wasserstein distance for two PDFs $\rho_1(\boldsymbol{s}, \boldsymbol{r}, t)$ and $\rho_2(\boldsymbol{s}, \boldsymbol{r}, t)$ is

$$J_{W_p}^{p}\left(\rho_1, \rho_2\right) = \min_{T}\int de c_p^p\left(\boldsymbol{e}, \boldsymbol{E}_{\rho_1\rho_2}(\boldsymbol{e})\right)\rho_2(\boldsymbol{e}) \tag{3}$$

subject to the constraint $\boldsymbol{E}_{d_1 d_2} \in \boldsymbol{T}$ the set of maps on $\boldsymbol{e}$ that rearrange ρ_2 to ρ_1.

e denotes a data coordinate space vector and c_p denotes the Lp distance between vectors in the data coordinate space. Equations above seek at the minimum cost to transport mass from ρ_2 to ρ_1 from the c_p^p point of view. Note that with seismic data being recorded in space and time, these dimensions need to be normalized within the Lp distance with a ratio involving an apparent velocity (Messud and Sedova, 2019).

An important aspect of the OT formalism is that ρ_1 and ρ_2 are required to be PDFs, i.e. positive with equal masses, implying that OT cannot be readily applied to seismic data. Yang et al., (2018) and Qiu et al., (2017) proposed using ad-hoc transformations of the observed and computed data to make them positive with the same mass. They chose the p=2 case in the first equation in this subsection, i.e. the squared 2-Wasserstein distance. Since solving equations above in the multi-dimensional data coordinate space case is computationally demanding, most of their applications consider a mono-dimensional coordinate space, where $\boldsymbol{e}$ is parameterized by time only (source and receiver positions being fixed). Then, equations above are solved for each trace independently.

Bearing in mind the properties of the 1-Wasserstein distance, Métivier et al. (2016a, 2016b, 2016c) chose p=1 in the first equation. As proposed by Métivier et al., (2016a), by reformulating the problem using the Kantorovich–Rubinstein (KR) dual formulation and adding a bounding constraint it is possible to use the seismic data directly without any transformation. Rather than minimizing the first equation for $\boldsymbol{E}_{d_1 d_2} \in \boldsymbol{T}$, we look for a λ-bounded 1-Lipschitz function,$\varphi(\boldsymbol{e}$, maximizing the so-called KR norm

$$J_{KR}\left(d_{obs}, d[\boldsymbol{m}]\right) = \max_{\varphi} \int d\boldsymbol{e}\varphi(\boldsymbol{e})\Delta d[\boldsymbol{m}](\boldsymbol{e}) \tag{4}$$

subject to

$$|\varphi\left(\boldsymbol{e}_1\right) - \varphi\left(\boldsymbol{e}_2\right)| \leq c_1\left(\boldsymbol{e}_1, \boldsymbol{e}_2\right) and |\varphi(\boldsymbol{e})| \leq \lambda. \tag{5}$$

φ is the solution of the maximization problem and can be demonstrated to represent the adjoint-source (Métivier et al., 2016b; Messud et al., 2021). The first constraint on φ in equation above is called 1-Lipschitz for the metric c_1. It imposes that changes in φ are sufficiently slow, which emphasizes low frequencies in φ . The second constraint, controlled by the parameter λ, makes it possible to stabilize the problem when seismic traces are used directly. This approach does not require any transformation of traces and has the advantage of an efficient numerical implementation.

FIELD DATA PROCESSING

The CaMI.FRS is located 190 km southeast of Calgary, near Brooks, Alberta. Figure 1a shows the location map of CaMI.FRS. The region is dominated by the Upper Cretaceous Belly River Group, including the Foremost, Oldman and Dinosaur Park formations. The Foremost formation is composed of inter-bedded sandstone, siltstone, carbonaceous shales and coal seams. The water-bed sandstone reservoir at depths of 295-301 m approximately, corresponding to the Basal Belly River Sandstone (BBRS) formation, is currently used as the target for CO_2 sequestration. The BBRS consists of several stacked composite regressive cycles dominated by shoreline sandstones and is directly overlain by mudstones, coals and fine sandstones of the McKay Coal Zone, which forms the cap rock for the reservoir. The dataset collected from linear sweep VP of a typical shot, which include data collected from

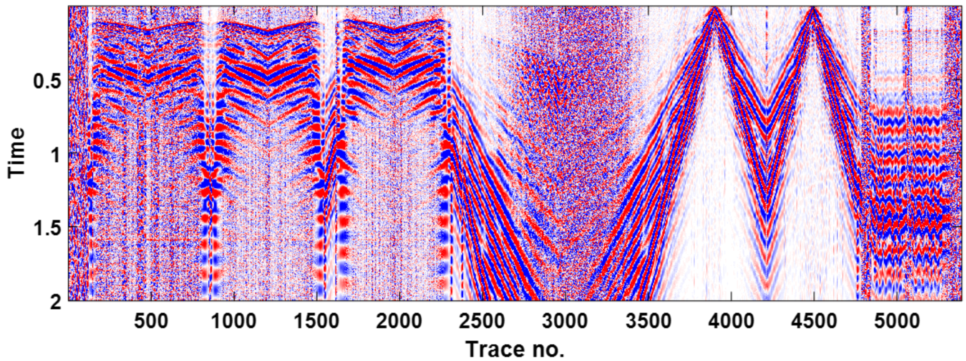

FIG. 2. The DAS data collected for line 13 using linear sweep VP.

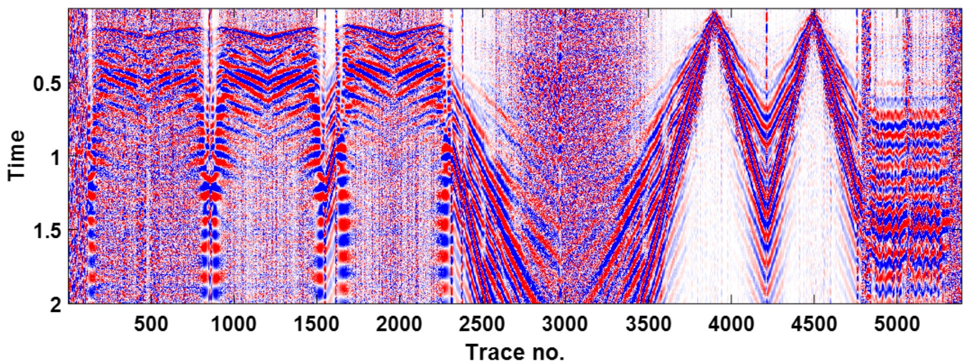

FIG. 3. The DAS data collected for line 13 using low-dwell sweep VP.

the straight fiber, the helical fiber, two well straight fiber, and one well helical fiber is shown in Figure 2. The dataset of a low-dwell sweep VP is shown in Figure 3.

From the seismograms, we can find there is no obvious waveform differences between these two datasets. The recording time of low-dwell dataset is a bit later than the linear-sweeping one.

The geometry of the ten shots data selected are shown in Figure 4.

In this figure, the fiber used for recording data is on the right of the three wells shown in green squares.

We firstly compared the two datasets collected from this year, shown in Figure 5 and Figure 6.

The slight differences between these two dataset are also the recording time.

From the comparison above, it is obvious that the datasets using the linear-sweep VP and low-dwell sweep VP are similar in waveforms. The differences of the recording time may be due to different source locations, difference wavelets or different sweeping start time.

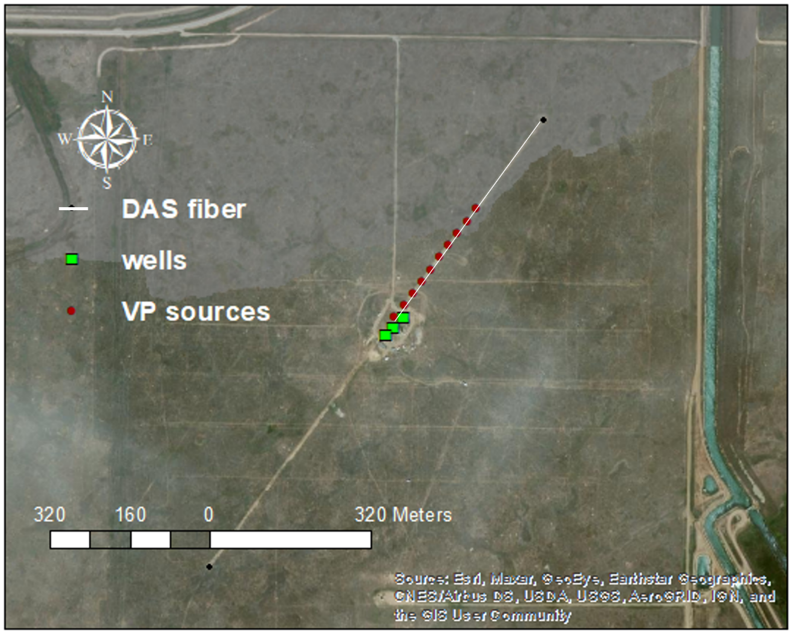

FIG. 4. The geometry of the selected ten shots and corresponding DAS fiber.

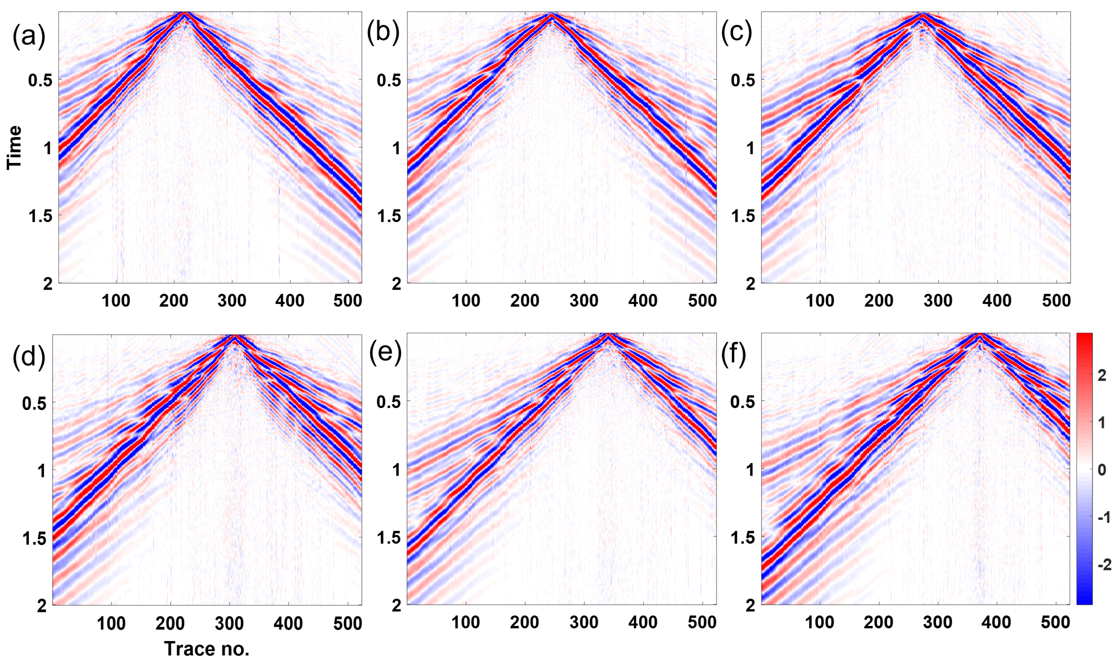

FIG. 5. The straight-fiber DAS data collected for 6 shots using linear sweep VP.

Conversion of DAS signals to displacement data

During DAS recording, the interrogator unit injects coherent laser pulses into the optical fiber. Phase changes of back-scattered light from consecutive pulses are measured. The phase changes are proportional to the changes in axial strain along finite sections of the fiber, referred to as *gauge length*. Therefore, the DAS system can be considered as a sequence

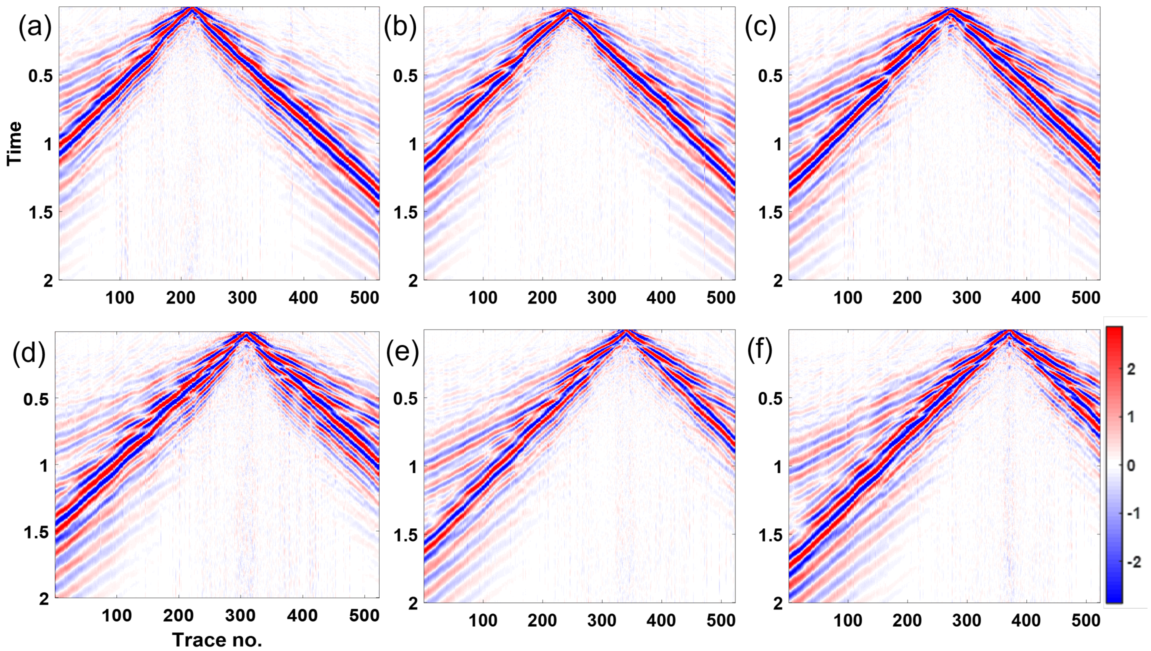

FIG. 6. The straight-fiber DAS data collected for 6 shots using low-dwell sweep VP.

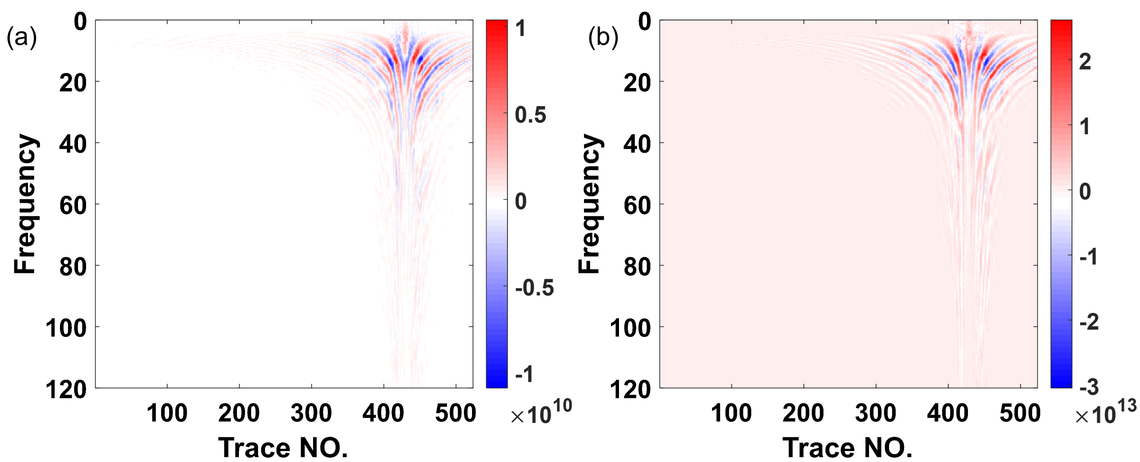

FIG. 7. The frequency spectra comparison of these two datasets.

of single-component seismic sensors, measuring strain rate variations with dense spatial sampling. The strain rate measurement of DAS can be expressed as

$$\partial_t \varepsilon_{xx} = \frac{1}{L}\left[v_x\left(z+\frac{L}{2}\right) - v_x\left(z-\frac{L}{2}\right)\right], \tag{6}$$

where v_x is the tangential particle velocity, L is gauge length, and z is the center of the gauge.

According to the adjoint-state method (or Born approximation) (Tromp et al., 2005; Liu and Tromp, 2006), the inputs for calculating sensitivity kernels in FWI are displacement fields of the seismic signals. The DAS-recorded strain rate data should be converted

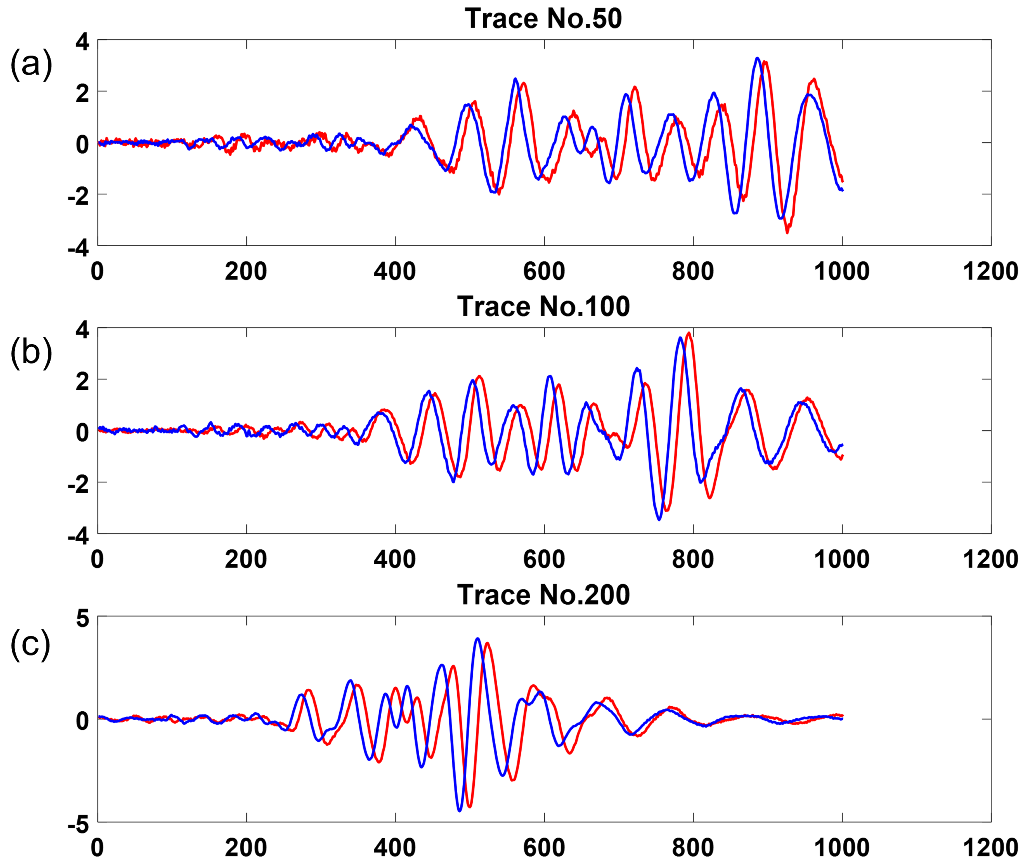

FIG. 8. The trace comparison of linear-sweep data and low-dwell sweep data.

into displacements for the inversion experiments. Converted DAS data can closely match geophone measurements in both amplitude and phase (Daley et al., 2016). In particular, Daley et al. (2016) showed that the strain rate signal can be converted to equivalent velocity units via scaling by apparent velocity. Considering a propagating harmonic plane-wave, its displacement and particle velocity fields in x direction are

$$u_x = Ue^{-\mathrm{i}\omega\left(t-\frac{x}{c}\right)}, \text{ and} \tag{7}$$

$$v_x = \frac{du_x}{dt} = -\mathrm{i}\omega Ue^{-\mathrm{i}\omega\left(t-\frac{x}{c}\right)}, \tag{8}$$

where U indicates amplitude of the plane-wave, c is apparent velocity, i is imaginary unit, and ω is angular frequency. Therefore, strain is given by (Benioff, 1932; Mikumo and Aki, 1964)

$$\varepsilon_{xx} = \frac{\partial u_x}{\partial x} = \partial_t u_x \frac{dt}{dx} = \pm\frac{\partial_t u_x}{c}, \tag{9}$$

where "$\pm$" is the direction of wave propagation. Therefore, the DAS signal can be converted to geophone-signal units via scaling of apparent velocity followed by time integrations.

Wavelets and filtering

The autocorrelation of the low-dwell sweep is shown in Figure 9, which is also a zero-phased Klauder wavelet.

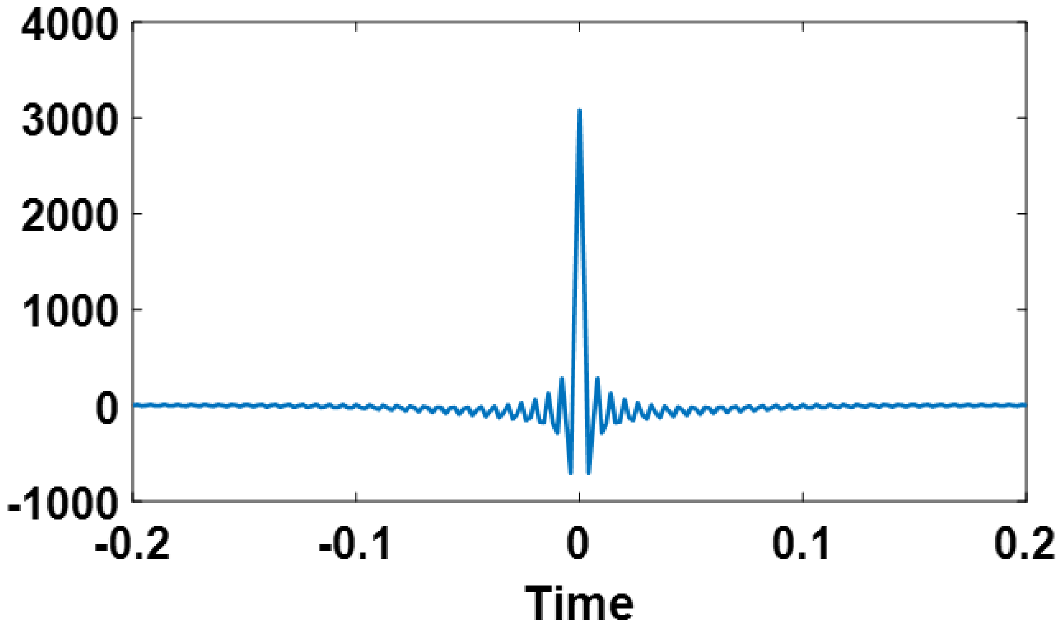

FIG. 9. The autocorrelation of the low-dwell sweep.

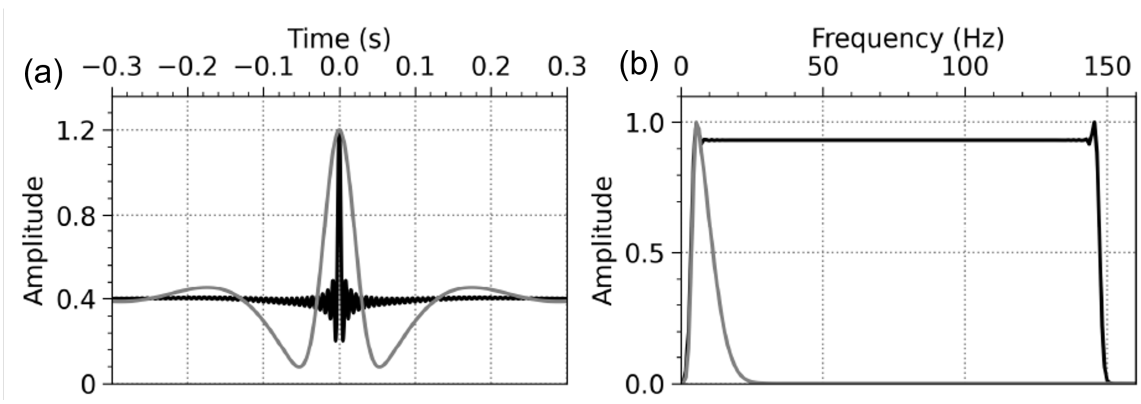

FIG. 10. The original and filtered Klauder wavelet.

In the processing of the FWI, the wavelet and observing data were filtered to make sure the synthetic and observing data are using the same frequency bands.

Preliminary inversion results

We conducted the inversion with several steps. Low-dwell DAS data were used in the FWI processing.

At first, we conducted surface-wave full waveform inversion using the fundamental-mode Rayleigh waves with optimal transport method. The initial model and inverted Vs model is shown in Figure 11 and Figure 12

Based on the obtained the Vs model, a VSP FWI was conducted using the DAS data collected from the straight fiber in the two wells. The inverted Vp model is shown in

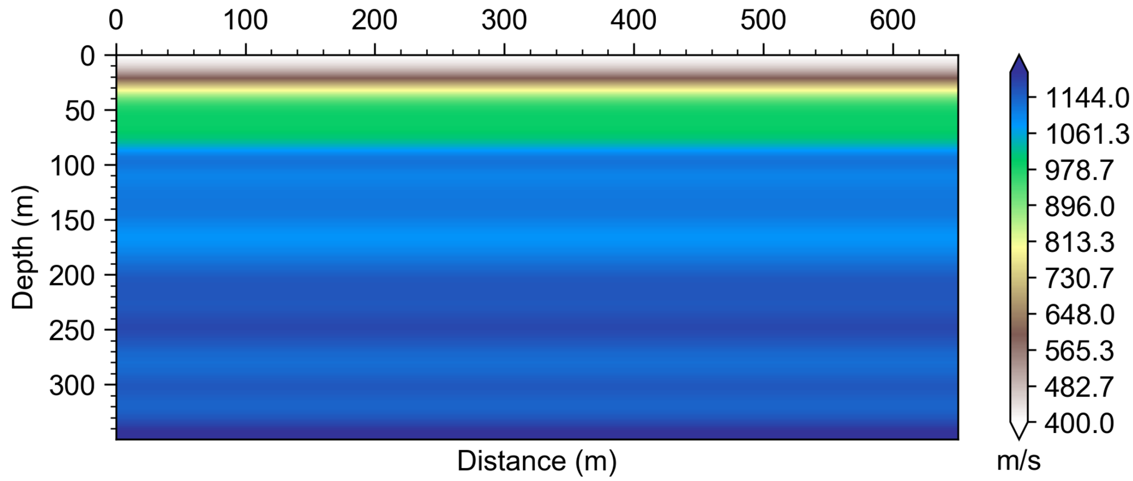

FIG. 11. The initial model for surface-wave FWI.

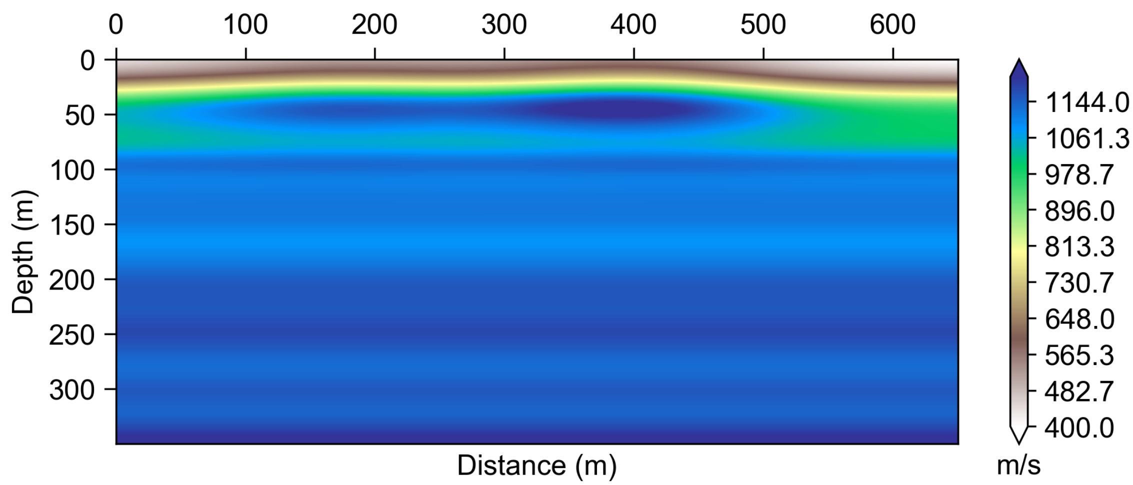

FIG. 12. The inverted Vs model of surface-wave FWI.

Figure 13. O shown in the x-axis represents the NE end point of the DAS trench fiber. These are the preliminary inversion results of the surface-wave FWI and VSP FWI. Given more time, a more detailed and through real data processing will be implemented.

CONCLUSIONS

The two datasets collected using linear sweep VP and low dwell sweep VP have the same frequency range through comparison. Their waveforms are different slightly. This is may be due to the difference of the wavelet or changes of the source locations. If the difference is caused by wavelet changes, a better wavelet estimation should be conducted before the inversion. If it is caused by the source location changes, a calibration on both datasets should be done.

For surface-deployed straight fiber, only single-component high-amplitude surface wave data are collected. Thus, a rough Vs profile with limited depth can be obtained through a surface-wave FWI. However, engineering and researchers are more interested in the Vp

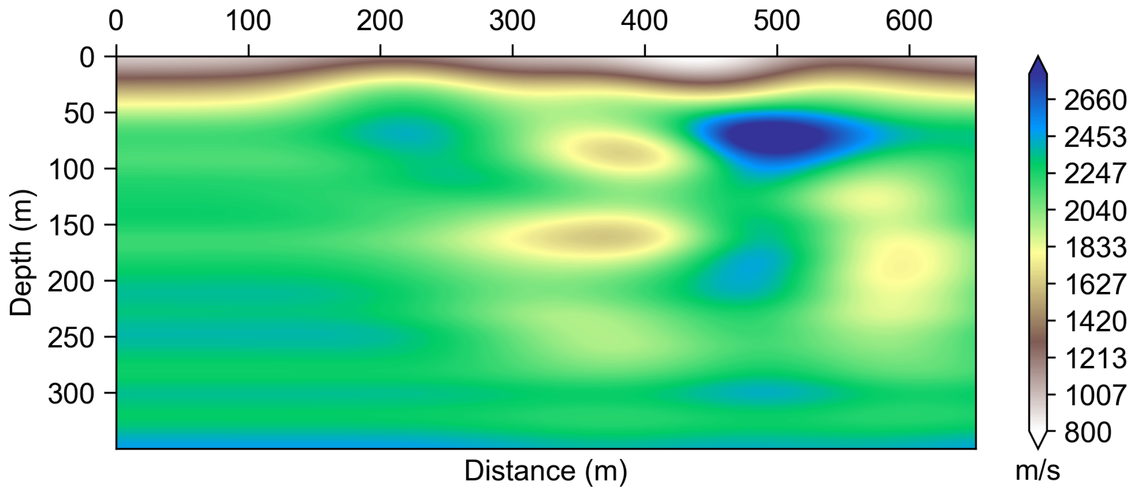

FIG. 13. The inverted Vp model of VSP FWI.

profile in some cases. The straight-fiber DAS data collected from the wells can help invert the Vp profile with a high resolution. In this study, we adopted a sequential inversion strategy to firstly invert the Vs using surface-wave FWI with optical transport. Secondly, we conducted VSP FWI using the DAS datasets from the two wells to invert Vp based on the Vs profile obtained from the first round FWI.

DISCUSSION

There are some detailed questions in the inversion with respect to DAS data. With this type of real data processing, many aspects need to be considered during the inversion. For example, in surface wave full-waveform inversion, though the data has maximal sensitivity with respect to Vs rather than other model parameters. The accurate of other parameters including Vp and density still have influence on the inversion result of Vs. The strategy of dealing with multimode surface waves, and the consideration of attenuation estimation also have impacts on the inversion accuracy of Vs. If we convert the DAS data to displacement or velocity data using a traditional method, the polarity reversal problem should also be addressed. Another challenge for joint surface-wave and VSP FWI is that the resolutions of inverted models are different. The accurate building of initial model, frequency filtering, and wavelet estimation can all influence the inversion result. A good inversion result of the real dataset need to consider all the influencing factors above and need to make sure all the model parameters are well estimated through FWI or not.

ACKNOWLEDGEMENTS

We thank the sponsors of CREWES for continued support. This work was funded by CREWES industrial sponsors and NSERC (Natural Science and Engineering Research Council of Canada) through the grant CRDPJ 543578-19. The data were acquired through a collaboration with Carbon Management Canada.

REFERENCES

Ajo-Franklin, J. B., Dou, S., Lindsey, N. J., Monga, I., Tracy, C., Robertson, M., Tribaldos, V. R., Ulrich, C., Freifeld, B. M., Daley, T. M., and Li, X., 2019, Distributed acoustic sensing using dark fiber for near-surface characterization and broadband seismic event detection: Scientific Reports, **9**, 1–14.

Benioff, H., 1932, A new vertical seismograph: Bulletin of the Seismological Society of America, **22**, No. 2, 155–169.

Daley, T. M., Miller, D. E., Dodds, K., Cook, P., and Freifeld, B. M., 2016, Field testing of modular borehole monitoring with simultaneous distributed acoustic sensing and geophone vertical seismic profiles at Citronelle, Alabama: Geophysical Prospecting, **64**, 1318–1334.

Dou, S., Lindsey, N. J., Wagner, A. M., Daley, T. M., Freifeld, B., Robertson, M., Peterson, J., Ulrich, C., Martin, E. R., and Ajo-Franklin, J. B., 2017, Distributed acoustic sensing for seismic monitoring of the near surface: a traffic-noise interferometry case study: Scientific Reports, **7**, 11,620.

Gordon, A., and Lawton, D., 2018, Vsp processing of distributed acoustic sensing and geophone data at cami field research station, newell county, alberta, *in* GeoConvention 2018, Expanded Abstracts.

Gordon, A., and Lawton, D. C., 2017, Zero offset vsp processing of fiber optic cable (das) and geophone array at the cami field research station, *in* CREWES Annual Reports.

Hall, K. W., Lawton, D. C., Daley, T., Freifeld, B., and Cook, P., 2017, Source distance and source effort on das data, *in* CREWES Annual Reports.

Hall, K. W., Lawton, D. C., Daley, T. M., Freifeld, B. M., and Cook, P., 2018, Effect of source effort and source distance on optical-fibre data at cami. frs, newell county, alberta, *in* SEG Technical Program Expanded Abstracts 2018, Society of Exploration Geophysicists, 206–210.

Jin, G., and Roy, B., 2017, Hydraulic-fracture geometry characterization using low-frequency DAS signal: The Leading Edge, **36**, 962–1044.

Lawton, D., Bertram, M., Hall, K., and Bertram, K., 2015, New approaches to seismic monitoring at the brooks field research station, *in* CREWES Annual Reports.

Lawton, D., Hall, K., and Gordon, A., 2018, Advances in das seismic monitoring for co2 storage, *in* 2018 SEG International Exposition and Annual Meeting, OnePetro.

Lawton, D. C., Dongas, J., Osadetz, K., Saeedfar, A., and Macquet, M., 2019, Development and analysis of a geostatic model for shallow co2 injection at the field research station, southern alberta, canada: Geophysics and Geosequestration. Cambridge University Press, Cambridge, **280**, 296.

Lindsey, N. J., Dawe, T. C., and Ajo-Franklin, J. B., 2019, Illuminating seafloor faults and ocean dynamics with dark fiber distributed acoustic sensing: Science, **366**, 1103–1107.

Lindsey, N. J., Rademacher, H., and Ajo-Franklin, J. B., 2017, On the broadband instrument response of fiber-optic DAS arrays: Journal of Geophysical Research: Solid Earth, **125**, e2019JB018,145.

Liu, Q., and Tromp, J., 2006, Finite-Frequency Kernels Based on Adjoint Methods: Bulletin of Seismological Society of America, **96**, 2383–2397.

Masoudi, A., Belal, M., and Newson, T. P., 2013, A distributed optical fibre dynamic strain sensor based on phase-OTDR: Measurement Science and Technology, **24**, 085,204.

Masoudi, A., Lopez, J., Potters, H., Mestayer, J., Cox, B., Kiyashchenko, D., Wills, P., Grandi, S., Hornman, K., Kuvshinov, B., Berlang, W., Yang, Z., and Detomo, R., 2014, Distributed acoustic sensing for reservoir monitoring with vertical seismic profiling: Geophysical Prospecting, **62**, 679–692.

Mikumo, T., and Aki, K., 1964, Determination of local phase velocity by intercomparison of seismograms from strain and pendulum instruments: Journal of Geophysical Research, **69**, No. 4, 721–731.

Nocedal, J., and Wright, S. J., 2006, Numerical Optimization: Springer.

Plessix, R. E., 2006, A review of the adjoint-state method for computing the gradient of a functional with geophysical applications: Geophysical Journal International, **167**, 495–503.

Posey, J. R., Johnson, G., and Vohra, S., 2000, Strain sensing based on coherent Rayleigh scattering in an optical fibre: IEEE Electronics Letters, **36**, 1688–1689.

Spackman, T., and Lawton, D. C., 2018, Processing and analysis of data recorded from a buried permanent seismic source, *in* CREWES Annual Reports.

Stork, A., Nixon, C., Hawkes, C., Birnie, C., White, D., Schmitt, D., and Roberts, B., 2018, Is co2 injection at aquistore aseismic? a combined seismological and geomechanical study of early injection operations: International Journal of Greenhouse Gas Control, **75**, 107–124.

Tromp, J., Tape, C., and Liu, Q., 2005, Seismic tomography, adjoint methods, time reversal, and banana-doughnut kernels: Geophysical Journal International, **160**, 195–216.